Received: 4 February 2025 | Accepted: 6 August 2025

DOI: 10.1111/mice.70051

INDUSTRIAL APPLICATION

COMPUTER-AIDED CIVIL AND INFRASTRUCTURE ENGINEERING WILEY

Virtual sensing of seismic floor responses for rapid prioritization of critical equipment inspection in nuclear power plants

Jingoo Lee[1] | **Seungjun Lee**[2] | **Young-Joo Lee**[1] | **Jaebeom Lee**[2,3]

[1]Department of Civil, Urban, Earth, and Environmental Engineering, Ulsan National Institute of Science and Technology, Ulsan, Republic of Korea

[2]Division of Physical Metrology, Korea Research Institute of Standards and Science, Daejeon, Republic of Korea

[3]Precision Measurement Major, University of Science and Technology, Daejeon, Republic of Korea

Correspondence
Young-Joo Lee, Department of Civil, Urban, Earth, and Environmental Engineering, Ulsan National Institute of Science and Technology, Ulsan 44919, Republic of Korea.
Email: ylee@unist.ac.kr

Jaebeom Lee, Division of Physical Metrology, Korea Research Institute of Standards and Science, 267 Gajeong-ro, Yuseong, Daejeon, Republic of Korea; Precision Measurement Major, University of Science and Technology, 217 Gajeong-ro, Yuseong-gu, Daejeon, Republic of Korea.
Email: jblee@kriss.re.kr, jblee@ust.ac.kr

Funding information
National Research Foundation of Korea, Grant/Award Numbers: 2021R1C1C2008770, RS-2022-00144434

Abstract

Critical equipment in nuclear power plant auxiliary buildings such as control cabinets, panels, transformers, and diesel generators often malfunction before structural damage occurs, demanding rapid post-earthquake inspection prioritization. However, direct walkdown inspection or dense sensor networks are impractical due to restricted accessibility in radiological zones and the high costs associated with maintenance. To address this, we propose a residual convolutional network-based virtual sensing framework that supports urgent inspection prioritization by predicting acceleration at 139 locations from a single high-quality seismometer. The model employs six residual blocks with progressively downsized kernels to capture multi-scale features, while skip connections prevent vanishing gradients. Trained on artificial earthquakes with 10 dB noise and validated against unseen Next Generation Attenuation-West 2 ground motions matched to Nuclear Regulatory Commission Regulatory Guide 1.60 and Korean uniform-hazard spectra, the model achieves a maximum mean absolute percentage error of 0.44%–0.59% for noise-free case and ≤4.23% at 10 dB, demonstrating robust generalization. The resulting rapid, noise-tolerant virtual sensor network enables actionable equipment-level decision making in nuclear facilities at a fraction of conventional monitoring cost.

1 | INTRODUCTION

Worldwide experience with earthquakes has shown that critical equipment in auxiliary buildings, such as electrical control cabinets, power-distribution panels, transformers, and emergency diesel generators, is often the first element to malfunction and trigger a reactor shutdown, even when primary concrete structures remain elastic. For example, during the 2016 Gyeongju earthquake, the earthquake did not pose a structural safety threat, but peak ground

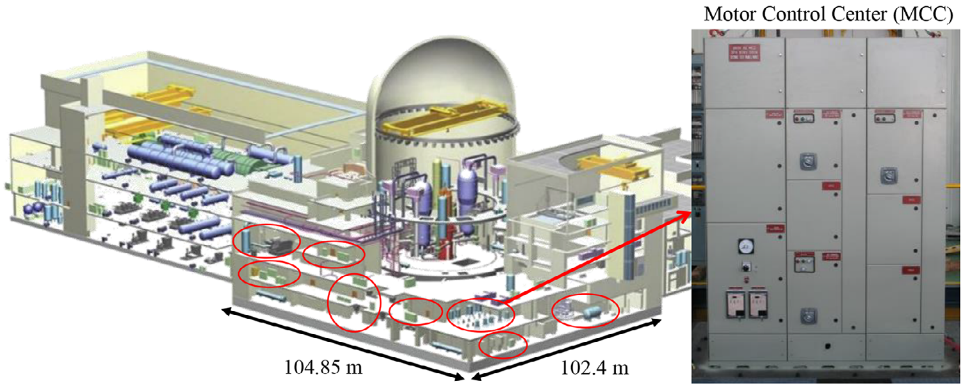

FIGURE 1 Advanced Power Reactor (APR) 1400 and the locations of motor control center (MCC; also referred to as cabinets).

accelerations (PGAs) at Wolsong Units 1–4 exceeded the operating-basis limit, leading to a manual shutdown and a plant-wide inspection of hundreds of cabinets and panels (Choun & Kwon, 2018). Similar equipment interruptions have been reported across multiple nuclear power plants (NPPs) following earthquakes. At the North Anna Nuclear Generating Station during the 2011 Virginia earthquake, switch faults and the failure of one diesel generator accompanied an automatic reactor trip (NRC, 2011). In 2007, a main transformer caught fire at Kashiwazaki-Kariwa following the Niigata-Chuetsu-Oki earthquake (IAEA, 2007). At Onagawa in 2011, a high-voltage distribution panel ignited in the turbine building during the Tōhoku earthquake (Japan Nuclear Safety Institute, 2011). More recently, in 2019, the Le Teil earthquake prompted a preventive shutdown of three units at the Cruas-Meysse Nuclear Power Plant to allow for cabinet and switchgear inspections (ASN, 2020). Previously mentioned incidents and requirements motivated a monitoring strategy focused not only on structural collapse but also on the rapid post-quake prioritization of critical equipment inspections. However, as shown in Figure 1, critical equipment is distributed across multiple locations within the NPP. Therefore, to determine whether such equipment might be damaged, it is necessary to monitor the structural response at each location. According to Nuclear Regulatory Commission (NRC) guidelines, a walkdown inspection, which involves the physical verification by on-site personnel, must be conducted regardless of earthquake intensity (Kassawara, 2012), which is time-consuming.

Acquiring the rich response data needed for such prioritization remains challenging. Physical sensors have been widely employed to capture seismic responses and assess structural conditions. Despite their extensive use, physical sensors are vulnerable to sudden malfunctions, measurement errors, and high installation and replacement costs (Yoon, 2022; Zaidan et al., 2020). Traditional sensors, such as dense fiber-optic grids (Hampshire & Adeli, 2000) and wireless smart nodes (Amezquita-Sanchez et al., 2018), might be expensive and fragile under extreme conditions underscoring the need for more flexible and resilient monitoring solutions.

Virtual sensors, or software-based sensors, estimate physical quantities at un-instrumented locations without requiring direct installations, offering a promising alternative (Martin et al., 2021). Previous studies have demonstrated their feasibility: convolutional neural network (CNN) methods successfully reconstructed structural vibrations from limited measurements (Sun et al., 2017). Recent CNN-based advances in earthquake engineering, including quantum-CNN damage classification (Bhatta & Dang, 2024), and explainable-Artificial inteligence (AI) seismic response interpretation (Shabbir et al., 2025), underscore the approach's versatility for capturing complex earthquake-induced patterns. Furthermore, physics-informed autoencoders have accurately predicted environmental phenomena from sparse sensor data (Gao et al., 2024). Virtual sensors not only reduce installation and maintenance costs but also improve data reliability by mitigating noise (Moreau et al., 2008) and compensating for sensor drift (Rashvand et al., 2014; Stavropoulos et al., 2023). Their flexibility allows updates without requiring additional physical interventions. Recent study also suggests that combining finite element (FE) simulations with machine learning can further improve model accuracy, especially in structural applications (Pereira et al., 2020). Virtual sensing techniques have been successfully applied across diverse domains, including chiller efficiency estimation (Alonso et al., 2021), vehicle dynamics (Ghosh et al., 2018), indoor air-pollution monitoring (Gabriel & Auer, 2023), smart farming (Patrizi et al., 2022), and structural strain estimation from acceleration data (Gulgec et al., 2020).

However, most previous studies have focused on replacing individual sensors or covering limited spatial domains. Multi-location virtual sensor systems capable

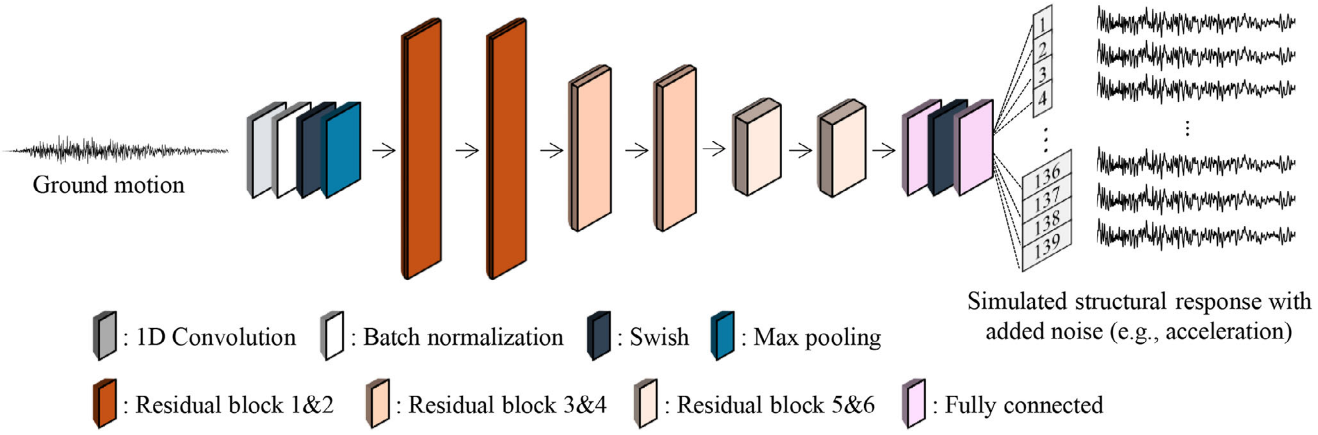

FIGURE 2 Architecture of proposed deep learning model.

of reconstructing widespread responses across complex structures remain relatively underexplored. Recent advances in operator-learning approaches have opened new possibilities for virtual sensing. Techniques such as deep operator networks can estimate structural responses at un-instrumented areas using information from a small number of accessible sensors, thereby reducing deployment complexity while maintaining high monitoring fidelity (Wüest et al., 2024). Operator-learning methods such as the Fourier neural operator applied to bridge responses (Kaewnuratchadasorn et al., 2024a) offer promising avenues for future integration with CNN-based surrogate models. Addressing the need for more scalable solutions also involves the adoption of powerful learning mechanisms, including neural dynamic classifiers (Rafiei & Adeli, 2017), dynamic ensemble frameworks (Alam et al., 2020), and transformer-based architecture (Gao et al., 2023), which demonstrated strong capabilities in modeling complex spatiotemporal interactions. While these emerging operator-learning approaches have demonstrated impressive performance in modeling continuous physical fields, their application to build virtual sensors at multiple locations for complex structural systems with sparse, noisy, and spatially discrete measurements has not yet been thoroughly investigated.

This study addresses challenges inherent to seismic monitoring by developing a deep residual CNN method capable of simultaneously predicting seismic responses at multiple locations. In particular, a CNN architecture designed to mitigate the vanishing gradient problem, common during the training of deep learning models, was introduced and applied to the auxiliary building of the Advanced Power Reactor (APR) 1400, an NPP designed by Korea Electric Power Corporation. Artificial earthquake (AEQ) data were used to train the proposed model, and to validate its performance, earthquake records from the Next Generation Attenuation (NGA) West 2 databased (Ancheta et al., 2014), matched with the NRC 1.60 spectrum and the Korea Uniform Hazard Spectrum (UHS) proposed by the Korea Atomic Energy Research Institute (Choi et al., 2003), were utilized.

2 | PROPOSED METHOD

2.1 | One-dimensional (1D) CNN

A 1D CNN is a type of conventional CNN for analyzing sequence data, such as time series data (Choi et al., 2024). The fundamental objective of a 1D CNN is to extract meaningful features and patterns from input sequences using convolutional processes. In a 1D CNN, the convolution operation involves sliding a kernel (also known as a filter) across the input sequence. This kernel is a learnable array of weights applied to a subsection of input data to produce a feature map. The feature map highlights important local patterns in the input data, such as trends or spikes in time-series signals.

The convolution operation can be mathematically expressed as (Ige & Sibiya, 2024):

$$(f*k)(t) = \sum_{i=0}^{m-1} f(t+i)\cdot k(i)$$

where f is the input sequence, k is the kernel, and m is the kernel size. t represents the index of the output sequence where the convolution result is being calculated, and i is the index within the kernel, iterating from 0 to $m-1$ to compute the sum of element-wise multiplications between the kernel $k(i)$ and the corresponding portion of the input sequence $f(t+i)$.

1D CNNs offer several advantages for processing time-series data (Bai et al., 2018; Mittelman et al., 2015). They are computationally more efficient than RNNs and LSTMs, owing to their simpler operations. They can process the entire input sequence in parallel, thereby enhancing computational speed. By focusing on local patterns through convolution, 1D CNNs can effectively capture important features in sequence data. More detailed information on 1D CNNs can be found in Kiranyaz et al. (2021).

2.2 | Residual learning

The key of residual learning is the introduction of residual connections, also known as skip connections, which improve the flow of gradients through the network during training. These connections enable the network to bypass one or more layers and directly pass the input to a later layer, thereby facilitating more effective training in deep architectures. In general, the output at the Lth residual block can be written as

$$x_L = x_l + \sum_{j=L}^{L-1} F\left(x_j\right)$$

where L is the index of a deeper block and l is the index of a shallower one. This equation shows that the input from a shallow block l directly propagated to the deeper block L, ensuring efficient information flow across layers. The partial derivative of the loss function ε with regard to the input of the lth residual block is given by:

$$\frac{\partial \varepsilon}{\partial x_l} = \frac{\partial \varepsilon}{\partial x_L}\frac{\partial x_L}{\partial x_l} = \frac{\partial \varepsilon}{\partial x_L}\left(1 + \frac{\partial}{\partial x_l}\sum_{j=l}^{L-1} F\left(x_j\right)\right)$$

$$= \frac{\partial \varepsilon}{\partial x_L} + \frac{\partial \varepsilon}{\partial x_L}\frac{\partial}{\partial x_l}\sum_{j=l}^{L-1} F\left(x_j\right)$$

Even if the gradients of the $F(x_j)$ terms are small, the total gradient $\frac{\partial \varepsilon}{\partial x_l}$ avoids vanishing due to the contribution from $\frac{\partial \varepsilon}{\partial x_L}$. More details can be found in He et al. (2016).

2.3 | Proposed model

To predict seismic acceleration responses across multiple structural locations simultaneously, this study proposes a deep residual 1D CNN to extract multi-scale temporal features from ground motion. The architectural design is motivated by the temporal and spectral characteristics of earthquake signals and the dynamic behavior of complex structures. A schematic overview of the proposed network is illustrated in Figure 2, while the internal structure of each residual block is detailed in Figure 3. The model accepts a time series input $X = [x_1, x_2, \ldots, x_T] \in R^T$, representing seismic acceleration records, where T is the number of time steps. The input sequence is normalized using z-score normalization:

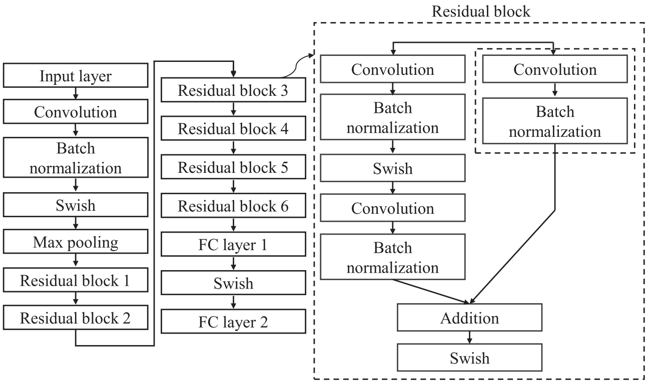

FIGURE 3 Architecture of deep learning model and enlarged view of residual block architecture.

$$x_t' = \frac{x_t - \mu_x}{\sigma_x}\ for\ t = 1, \ldots, T$$

where μ_x and σ_x are the mean and standard deviation of the input sequence, respectively. This normalization ensures that the input distribution is centered around zero with unit variance, facilitating more stable and efficient training. The normalized sequence is first processed by an initial 1D convolutional feature extractor composed of a convolutional layer with kernel size $k = 100$, followed by batch normalization, a Swish activation function, and a max pooling layer. Given a fixed sampling interval of 0.01 s, the initial convolutional kernel (size = 100) covers 1.0 s of input signal, enabling the extraction of long-duration, low-frequency components from the raw seismic input. The Swish function is defined as

$$Swish\left(\varkappa\right) = \varkappa \cdot \sigma\left(\varkappa\right) = \frac{\varkappa}{1 + e^{\varkappa}}$$

where $\sigma(\varkappa)$ denotes the sigmoid function. This non-monotonic activation function is known to preserve small gradients and enhance generalization performance in deep networks (Ramachandran et al., 2017). The batch normalization layer applied before each activation stabilizes the distribution of activations by re-centering and re-scaling (Ioffe & Szegedy, 2015; Santurkar et al., 2018):

$$BN\left(\varkappa\right) = \gamma \cdot \frac{\varkappa - \mu_B}{\sqrt{\sigma_B^2 + \epsilon}} + \beta$$

where μ_B and σ_B^2 are the mean and variance of the batch, γ and β are learnable parameters, and ϵ is a small constant for numerical stability. To preserve the temporal resolution after pooling, padding is added to ensure that the output sequence has the same length as the input, despite using a pool size of 3 and a stride of 1.

The extracted features are subsequently passed through six residual blocks, which are hierarchically grouped into three stages to facilitate multi-scale temporal feature learning. For clarity, the six residual blocks are denoted as ResBlock1 through ResBlock6, with ResBlock1–2 comprising the first stage, ResBlock3–4 the second, and ResBlock5–6 the final stage. Each stage employs a specific kernel size to extract distinct frequency bands from the seismic input. The first stage uses two residual blocks with a kernel size of 100, corresponding to 1 s of the input window (given a sampling interval of 0.01 s). These large kernels are effective for capturing long-duration, low-frequency features associated with global structural dynamics and low-frequency vibration. The second stage includes two blocks with a kernel size of 50 (0.5 s of input), designed to extract mid-frequency content. The final two blocks in the third stage adopt a kernel size of 10 (0.1 s of input), focusing on high-frequency, short-duration fluctuations. Each kernel acts similarly to a band-pass filter, responding to a range of frequencies centered around the inverse of the kernel duration (Farag et al., 2022). For instance, the kernel size of 100 emphasizes low-frequency features near 1 Hz, while still capturing adjacent spectral components within a broader band. This allows the network to extract rich multi-scale spectral features at each stage of the model.

Each residual block is composed of two 1D convolutional layers with batch normalization and Swish activation, followed by a shortcut connection to enable identity mapping. A schematic representation of this configuration is shown in Figure 3. The general formulation of a residual block output y is given by:

$$y = \phi\left(BN\left(W_2 * \phi\left(BN\left(W_1 * x\right)\right)\right)\right) + x$$

where W_1 and W_2 denote the convolution kernels of the first and second layers, $*$ represents 1D convolution, $\phi(\cdot)$ is the Swish activation, and x is the input feature map. In cases where the input and output dimensions differ, the shortcut connection is modified by applying a 1D convolutional projection:

$$y = \phi\left(BN\left(W_2 * \phi\left(BN\left(W_1 * x\right)\right)\right)\right) + W_s * x$$

where W_s is the kernel of the projection layer is used to align dimensions. This structure allows for stable training of deeper networks by preserving gradient flow and mitigating vanishing gradient issues.

To capture increasingly complex seismic features, the number of convolutional filters grows with depth: 32 in the first stage, 64 in the second, and 128 in the final stage. This design enhances the detection of intricate local features in later stages.

Following the residual stages, the final feature map is flattened and passed through two fully connected (dense) layers. The first dense layer has 512 units and applies the Swish activation to fuse the hierarchical features extracted from different stages. The output layer consists of 139 units, each representing the predicted acceleration response $\hat{y}$ at the ith structural node. Mathematically, the final output can be expressed as

$$\hat{y} = W_2^{(fc)} \cdot \phi\left(W_1^{(fc)} \cdot f + b_1\right) + b_2$$

where $f \in \mathbb{R}^d$ is the flattened feature vector, $W_1^{(fc)} \in \mathbb{R}^{512 \times d}$ $W_2^{(fc)} \in \mathbb{R}^{139 \times 512}$ and b_1, b_2 are the respective bias vectors. The resulting prediction vector $\hat{y} \in \mathbb{R}^{139}$ enables simultaneous inference of all nodal responses.

The hierarchical structure of the model, including variable kernel sizes and filter depths, reflects the physical behavior of structures under seismic excitation. Lower-frequency inputs with long durations tend to influence global modal responses, whereas higher-frequency components are associated with localized structural behavior (Boore & Goulet, 2019). By encoding this understanding into the network design, the model is well-suited to capture the full spectrum of structural response characteristics. Residual connections and batch normalization further enhance model stability and performance, ensuring robust and accurate learning over diverse seismic scenarios.

3 | APPLICATION EXAMPLE

3.1 | Overall framework

The overall framework for training the proposed model is illustrated in Figure 4. In this framework, measured ground motion data from the single seismometer located in bottom of the target NPP are used as input to the model. The model is trained to map the input ground acceleration (g) to the structural acceleration responses (in/s^2) at 139 locations within the auxiliary building. The FE analysis (FEA) data used for training was generated.

To reflect real-world measurement imperfections, synthetic noise was added to the structural responses generated from FEA. In practice, signals collected from physical sensors are inevitably contaminated by noise from sensor electronics, environmental conditions, and data acquisition systems. In this study, Signal-to-noise ratio (SNR) of

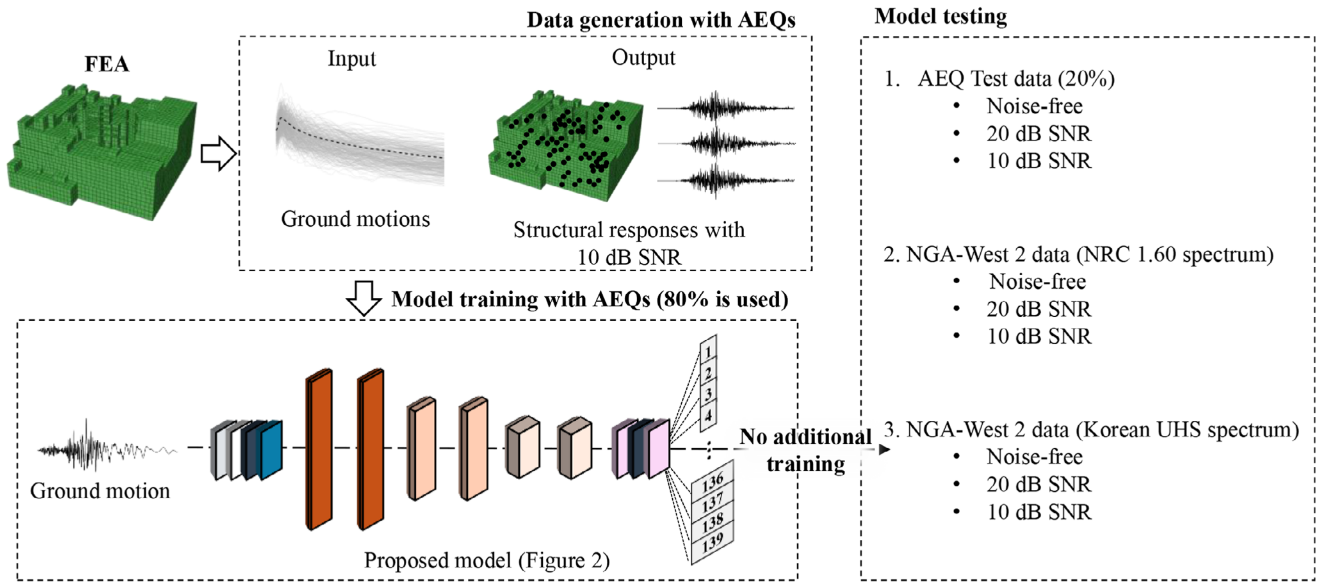

FIGURE 4 Overall framework. FEA, finite element analysis; NGA-West 2, Next Generation Attenuation West 2; UHS, Uniform Hazard Spectrum.

10 and 20 dB were applied to the simulated data to represent realistic sensing environments. An SNR of 20 dB corresponds to typical conditions encountered in general-purpose vibration sensing, while 10 dB represents more challenging scenarios characterized by weaker signals, low-cost sensors, or high environmental noise (Zhang & Wang, 2023). Incorporating these two noise levels allows the model to be evaluated not only under idealized but also under practical, field-representative conditions (Sercel, 2023).

A virtual sensing model was trained using AEQ data with a 10 dB SNR. Without any additional training or fine-tuning, the trained model was directly tested on real earthquake records (i.e., NGA–West 2 data). Three test scenarios were conducted on: (1) noise-free, (2) 20 dB SNR, and (3) 10 dB SNR.

3.2 | Target structure

The auxiliary building analyzed in this study surrounds the reactor building and, as shown in Figure 5, exhibits unsymmetrical geometry. Many critical equipment, including emergency diesel generators, motor-operated valves, control cabinets, and power distribution panels, are distributed across multiple floors and compartments. Its multi-story, irregular configuration increases structural complexity and presents significant challenges for sensor deployment. Installing physical sensors throughout the auxiliary building would require extensive cable routing, numerous penetration seals, and repeated maintenance activities under strict radiological safety protocols. These requirements impose considerable burdens in terms of installation, operation, and maintenance, particularly given the need for coordination across radiation-controlled areas, which increases costs, extends downtime, and complicates site procedures (IAEA, 2018).

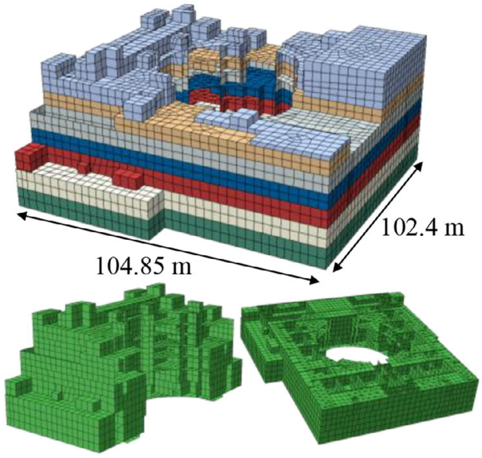

FIGURE 5 Finite element model of auxiliary building.

The irregular internal layout, characterized by intersecting corridors, non-uniform ceiling heights, and protruding structural elements, also generates localized vibration modes. Shaking-table experiments on cable-tray systems installed in auxiliary structures have demonstrated substantial floor-motion amplification in specific regions, highlighting the necessity of dense sensor networks to capture critical dynamic behaviors (Huang et al., 2017).

TABLE 1 Material properties of the auxiliary building.

	Concrete	Reinforcing bar	Steel
Elastic modulus (psi)	4.03×10^6	2.90×10^7	2.90×10^7
Density ($\mathrm{lbfs^2/in^4}$)	2.25×10^{-4}	7.35×10^{-4}	7.35×10^{-4}
Poisson ratio	0.17	0.30	0.30

Furthermore, studies on optimal sensor placement suggest that effective monitoring of such complex and asymmetrical structures would require hundreds of measurement points, each demanding dedicated data acquisition and installation provisions that are impractical under typical nuclear facility operating conditions (Bigoni et al., 2020).

Adding to these challenges, regulatory constraints often prohibit modifications to structural components, such as penetrations in walls or floors, without prior engineering review and approval. These safety requirements further limit the installing additional sensors in NPP environments.

To evaluate the seismic behavior of the auxiliary building, an FEM was developed using ABAQUS. The model represents a six-story building composed of 17,233 shell elements (S4R), with reinforcing bars modeled using layered shell elements. The base of the structure was fixed, and seismic excitation was applied in the x-directions through the time-history acceleration method using the base motion option in ABAQUS.

A linear material model was adopted to ensure computational efficiency while providing accurate predictions under design-level seismic conditions. This modeling choice is supported by nonlinear pushover analyses conducted on the auxiliary building in one horizontal direction. The pushover curve exhibited predominantly linear behavior up to a base shear coefficient of 2 g, which significantly exceeds both the design-level PGA of 0.3 g and the spectral acceleration at the fundamental period of the structure. These findings confirm that the auxiliary building can maintain elastic behavior well beyond the design-level earthquake, justifying the use of linear dynamic analysis in this study (Park et al., 2021). However, it is worth noting that such shaking can still cause malfunctions of critical equipment, such as control cabinets, panels, transformers, and diesel generators. Table 1 summarizes the material properties used in the model, including the elastic modulus, density, and Poisson's ratio for concrete, steel, and reinforcing bars.

The dynamic response of the auxiliary building was estimated using the modal superposition method (MSM) using 500 modes. By breaking down dynamic behavior into independent modal responses, MSM yields exact response estimations when applied to linear models.

3.3 | Virtual sensing model training

To develop the deep-learning model for virtual sensing, it is essential to begin with the collection of training data. AEQ generation has been widely adopted in recent research to create diverse and realistic seismic inputs. For example, Sirca and Adeli (2004) developed a neural network and wavelet-based model to generate artificial accelerograms. More recently, Miao et al. (2024) proposed a physics-guided neural network for producing response-compatible ground motions, while Shi et al. (2024) applied generative adversarial neural operators to synthesize broadband motions. These studies validated the credibility and usefulness of synthetic ground motions for training data generation in structural and seismic engineering applications.

In this study, synthetic ground motions were constructed using the stochastic ground motion model developed by Rezaeian and Der Kiureghian (2010). This model accurately captures the nonstationary characteristics of real earthquake records by modeling ground acceleration as modulated Gaussian processes with time-varying frequency and amplitude content. Key parameters governing the amplitude envelope and frequency evolution such as the Arias intensity I_a, significant duration D_{5-95}, midpoint of strong motion t_{mid}, central frequency ω_{mid}, rate of frequency change ω', and damping ratio ζ_f were estimated using predictive equations based on seismological variables.

For this purpose, site-specific input variables for the Ulsan region (i.e., the location of APR 1400 NPPs) were selected, corresponding to a strike-slip fault type ($F = 0$), moment magnitude $M = 6.0$, rupture distance $R_{rup} = 40$ km, and average shear-wave velocity in the top 30 m of soil $V_{s30} = 715$ m/s. These regional parameters were substituted into the regression models to generate the statistical characteristics necessary for synthetic ground motion generation. Numerous samples were then generated using these parameters to ensure adequate variability and generalizability for training the proposed virtual sensing model.

Generated AEQs were used to simulate the NPPs. The variety of AEQs ensured that the model could learn a wide range of seismic intensities and frequencies, making it robust and reliable for model performance. Figure 6 shows the spectra of the AEQs used in this application.

A broad-spectrum range is necessary to train the model to react accurately to earthquakes of different magnitudes and characteristics. This variety helps the model generalize better across different seismic scenarios, thereby improving its generalization performance. Three hundred AEQs were generated to form the dataset. To ensure a rigorous training and evaluation process, AEQs were divided into two sets: 240 AEQs were used for training the model and

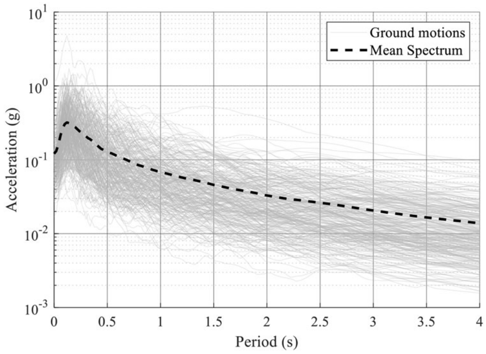

FIGURE 6 Spectrum of AEQs.

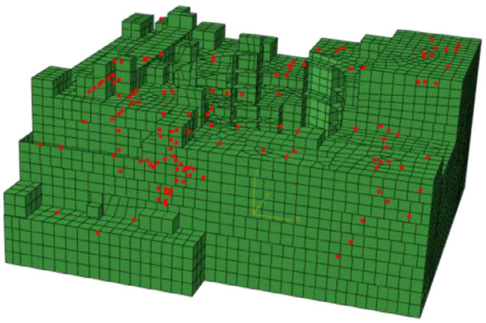

FIGURE 7 139 nodes selected for testing the virtualization performance.

the remaining 60 AEQs were used for testing. This separation is crucial for assessing the ability of the model to accurately predict structural responses under unseen seismic events. The training dataset was employed to optimize the model parameters, whereas the testing dataset was used to evaluate the generalization capability. During training, response data with an SNR of 10 dB is used to simulate harsher sensing environments. Note that noise is added only to the structural response data, not to the input ground motion i.e., AEQ. In the testing phase, the model—trained solely on 10 dB SNR data—is evaluated using response data with SNR levels of noise-free, 20 dB, and 10 dB to assess its generalization capability under varying noise conditions.

The training process involved introducing FEA data into a deep learning model, allowing it to learn the intricate patterns and responses of the auxiliary building under seismic loads. During training, the model parameters were adjusted through backpropagation to minimize the prediction error. Training was conducted over multiple epochs, where in each epoch, the entire training dataset was passed through the model multiple times to ensure that the model learned effectively from the data.

Several key techniques and settings are employed to enhance the training process: The model's hyperparameters were selected through grid search to ensure optimal performance. The search was conducted over learning rates [1.0×10^{-3}, 2.0×10^{-3}, 1.0×10^{-2}], L2 regularization factors [1.0×10^{-6}, 1.0×10^{-5}, 1.0×10^{-4}], and batch sizes [128, 250, 512]. The final configuration employed the Adam optimizer with an initial learning rate of 2.0×10^{-3}, up to 700 training epochs, and gradient clipping based on the global L2-norm. L2 regularization with a factor of 1.0×10^{-5} was applied to mitigate overfitting. A mini-batch size of 250 and epoch-wise data shuffling were used to prevent learning spurious patterns. A piecewise learning rate schedule reduced the learning rate by a factor of 0.1 every 300 epochs, enabling fine-tuning during later training stages. Training was performed using a computing setup with an Intel i9-14900K CPU and an NVIDIA GeForce RTX 4090 GPU.

3.4 | Virtual sensing model testing

The trained deep learning model was tested using 60 AEQs that were not included in the training dataset. The virtualization performance of the model was evaluated using the maximum mean absolute percentage error (mMAPE; Shin et al., 2018). This metric addresses the limitations of traditional methods such as MAPE and symmetric MAPE, particularly their inability to handle zero observations and their unsuitable evaluation of errors when the observed values are close to zero. The equation for mMAPE is shown in below.

$$mMAPE = \left\{ \frac{100}{n} \sum_{t=1}^{n} \frac{|A_t - F_t|}{|A|_{\max}} \right.$$

where A_t denotes the measurement value, F_t denotes the prediction value, $|A|_{\max}$ denotes the maximum absolute value of measurement values, and n is the number of the measurements.

Each earthquake simulation included a total of 3000-time steps, with an interval of 0.01 s per step. Unseen seismic events were utilized to thoroughly test the model's virtualization capability. Given the complexity of the auxiliary building, locations were randomly selected for performance testing. The locations of the randomly selected nodes are displayed in Figure 7. Figure 8 illustrates the mMAPE for 139 nodes randomly selected from the different floors of the auxiliary building.

As shown in Figures 8 and 9, the virtualization model accurately emulates the actual responses of the target structure with low mMAPE. The overall performance across 139 nodes was evaluated based on the average error of 60 AEQs, which demonstrated high accuracy of the model. The model trained under the 10 dB SNR condition

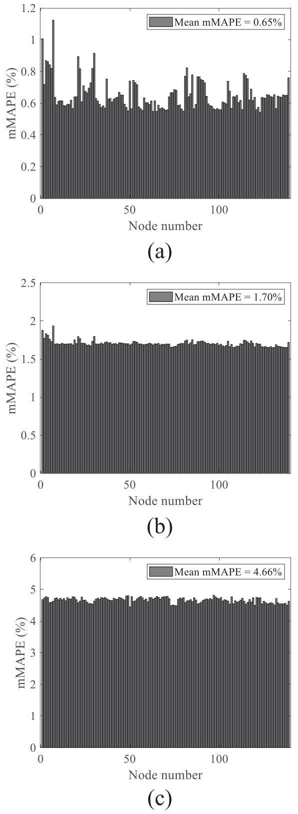

(a)

(b)

(c)

FIGURE 8 Maximum mean absolute percentage error (mMAPE) of the virtual sensing model for seismic responses at selected nodes under noise-free and noisy conditions (SNR of 10 and 20 dB).

is evaluated under three scenarios: (1) noise-free, (2) 20 dB SNR, and (3) 10 dB SNR. The prediction errors observed in each case are 0.65% for the noise-free condition, 1.70% for the 20 dB SNR condition, and 4.66% for the 10 dB SNR condition, which shows that the model, despite being trained on noisy data, best predicts the noise-free structural response that suggests that the model has effectively learned to denoise during the training process.

This high level of accuracy was further investigated by comparing the entire time history of the virtualization model predictions with the numerical analysis results obtained from the FEA. Figure 9 provides a detailed comparison of these two result sets, demonstrating the model's reliability across various locations. The model accurately predicts not only the overall responses but also the peak responses, which are important indicators in structural analysis. In Figure 9, the earthquake wave number indicates the sequence of ground motions included in the test data, while the node information represents the location number of the NPP among the 139 nodes. Although the selected nodes are located at low heights on the same floor, their response magnitudes vary significantly. This indicates the presence of local amplification effects within the auxiliary building and highlights the necessity of a multi-location virtual sensing model.

In the application example, the proposed model was trained using AEQs. Training was successful and resulted in a low error rate in test data. The model demonstrated excellent performance not only in overall time-series predictions but also in accurately predicting peak intervals. This indicates the efficiency of the model structure and confirms that the model was well-trained. The proposed model aims to virtualize physical sensors at multiple locations by utilizing a deep learning approach based on the CNN method. It also allows the estimation of multiple sensor outputs using measurement data from a single seismometer, thereby reducing the need for multiple physical installations. The successful training and testing outcomes suggest that the model can effectively emulate the behavior of physical sensors during earthquakes, providing reliable data for rapid safety assessment and decision making.

4 | CASE STUDY

Some previous studies have not rigorously validated seismic response prediction models using a substantial number of real earthquake records during testing (Huang & Chen, 2021; Oh et al., 2020). Instead, they often employed simplistic methods to divide available datasets into training and testing subsets as demonstrated in Section 3 of our study. In certain instances, the same earthquake records used for training were reused for validation, with only the intensity levels adjusted (Huang et al., 2003). As a result, critical factors influencing structural response amplifications, such as earthquake duration and dominant period, were not effectively accounted for (Oh et al., 2020). Strictly speaking, altering the intensity levels of the same earthquake records does not constitute entirely new data, making them insufficient for evaluating the robustness of virtual sensors. Additionally, several studies failed to clearly distinguish between earthquake records used for training neural networks and those reserved for validation (Morfidis & Kostinakis, 2017; Tezcan & Marin-Artieda, 2018), which can lead to substantial prediction errors (de Lautour & Omenzetter, 2009). Accordingly, this study seeks to assess the model's robustness using entirely different earthquake records, and this is demonstrated in this section.

When attempting to validate a model with real earthquake data, a typical approach would be to retrain the model using real earthquake data and then test it with a different set of real earthquake data (Zhang et al., 2019). In this case study, a deep learning model trained solely on AEQ data was validated against two distinct real

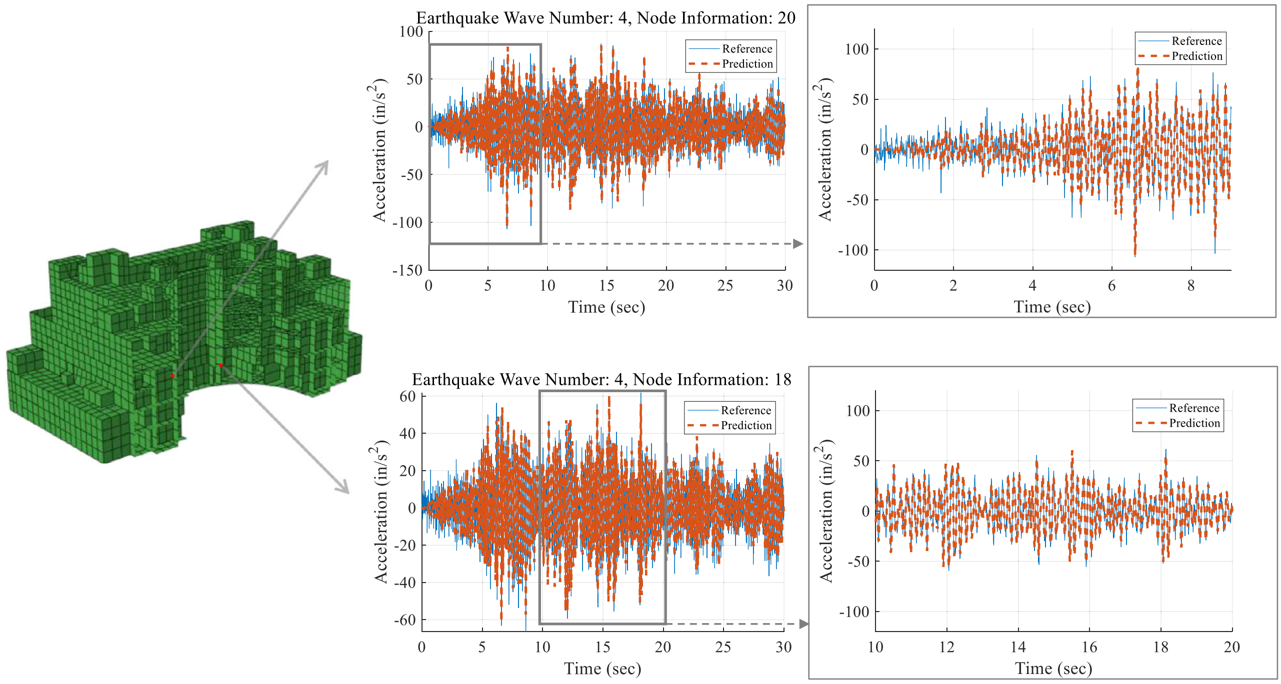

FIGURE 9 Virtualization results (10 dB SNR case) based on deep learning model for APR 1400; whole prediction results (left) and enlarged view (right).

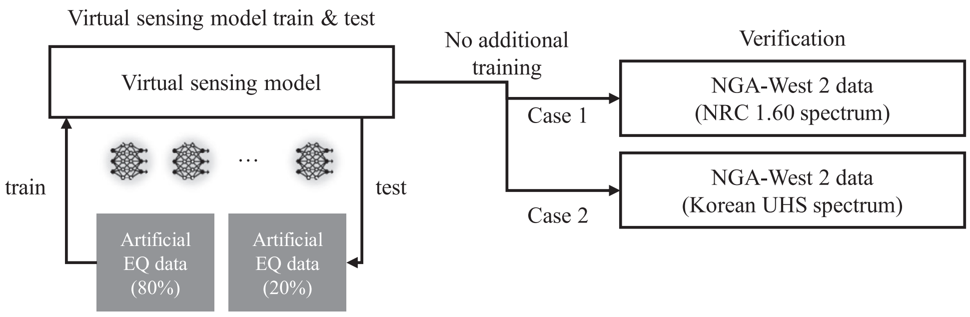

FIGURE 10 Schematic of case study 1 and 2. (*EQ: earthquake). NGA West 2, Next Generation Attenuation West 2; NRC, Nuclear Regulatory Commission; UHS, Uniform Hazard Spectrum.

earthquake scenarios without any additional fine-tuning. The test scenario was designed to evaluate the generalizability and robustness of the proposed virtual sensing model. The overall flow for further validation is illustrated in Figure 10.

As shown in Figure 10, a virtual sensing model was trained and tested using AEQ data previously. Without any additional training or fine-tuning with real EQ data, the trained model was directly applied to earthquake records from the NGA-West 2 database to evaluate its performance and robustness. The earthquake records utilized in Cases 1 and 2 are detailed in the Appendix A1. Specifically, 96 earthquake records are employed in Case 1, and 93 earthquake records are employed in Case 2. The processes of this evaluation are presented in Sections 4.1–4.4.

4.1 | Case 1: NGA West 2 database matching Regulatory Guide (RG) 1.60 spectrum

In the first validation case, earthquake records from the NGA West 2 database were utilized. These records were processed using the SeismoMatch software to match their spectra with the RG 1.60 spectrum, as defined by the NRC (2014). The purpose of this adjustment is to ensure that the earthquake records conform to a standardized spectral shape commonly used in the seismic design of nuclear facilities. As shown in Figure 11a, a deep learning model trained with AEQ data was applied to the Nuclear Regulatory Commission (NUREG) 1.60 spectrum, which was scaled to a PGA of 0.3 g.

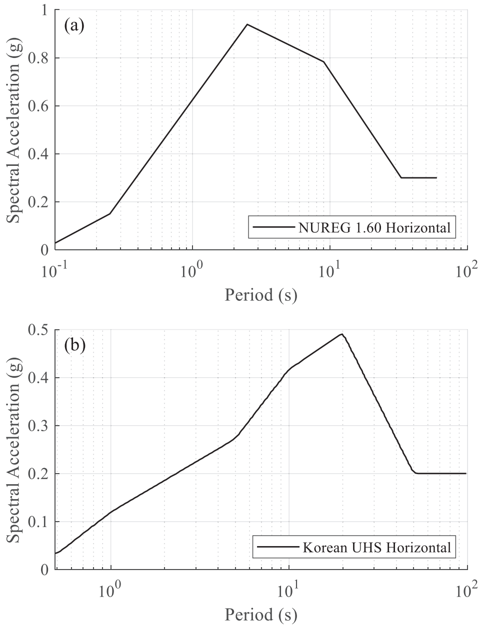

FIGURE 11 (a) NUREG 1.60 spectrum and matched earthquakes (Next Generation Attenuation [NGA]-West 2) and (b) Uniform Hazard Spectrum (UHS) spectrum of Korea and matched earthquakes (NGA-West 2).

Structural response data were obtained from the FEA of the auxiliary building of APR 1400 using the matched earthquake records, and the entire FEA dataset was used to test the pretrained virtual sensor model. The model performance was assessed by directly comparing between time-series predictions and FEA results, and by using the mMAPE.

4.2 | Case 2: NGA West 2 database matching Korean UHS

In the second validation case, earthquake records from the NGA West 2 database were utilized as well. However, in this case, the records were processed to match their spectrum with the Korean domestic spectrum, reflecting regional seismic characteristics. This case study aims to evaluate the model's performance using real earthquake data adjusted to local seismic conditions, thereby demonstrating its adaptability to region-specific seismic profiles. The deep learning model, trained with AEQ data, was applied to a UHS of Korea as shown in Figure 11b.

Structural response data were obtained from the FEA of the auxiliary building of APR 1400 using the matched earthquake data, and the FEA dataset was used to evaluate the pre-trained virtual sensor model. During the testing phase, the model performance was assessed by directly comparing time-series predictions and FEA results and also by using the mMAPE.

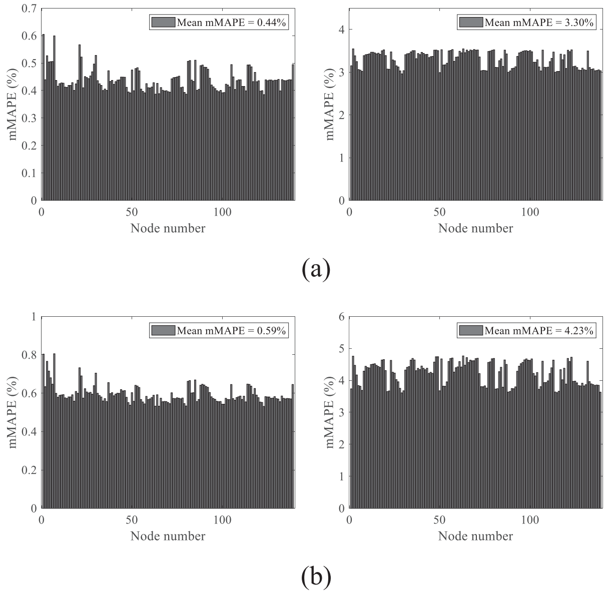

FIGURE 12 mMAPE for the noise-free (left) and 10 dB (right) cases in Case 1 (a) and Case 2 (b).

TABLE 2 Maximum mean absolute percentage error evaluated under various noise scenarios for Cases 1 and 2.

	Noise-free	20 dB	10 dB
Case 1	0.44%	1.19%	3.30%
Case 2	0.59%	1.55%	4.23%

4.3 | Prediction results

The results of Cases 1 and 2 demonstrate the effectiveness and reliability of the proposed residual 1D CNN-based virtualization method for predicting structural responses under different seismic conditions. The successful application of the model to real earthquake data from the NGA West 2 database, processed to match both the RG 1.60 spectrum and a Korean UHS, highlights its robustness and adaptability. The mMAPE across all nodes in the NPP is depicted in Figure 12.

Table 2 shows the mMAPE values. The model is trained using AEQ data with an SNR of 10 dB. This trained model is directly tested on both Cases 1 and 2 under three noise conditions: noise-free, 20 dB SNR, and 10 dB SNR. The prediction errors range from 0.44% to 0.59% under the noise-free condition, 1.19% to 1.55% under 20 dB SNR, and 3.30% to 4.23% under 10 dB SNR. These results demonstrate both high prediction accuracy and strong robustness to noise.

The prediction results for Cases 1 and 2 are illustrated in Figure 13a–d. In this figure, the earthquake wave number refers to the selected ground motion from the earthquake dataset, while the node information indicates the corresponding node number among the 139 nodes. The high level of accuracy observed in the predictions, both in the overall time-series and peak interval responses, highlights the model's strong generalization ability beyond the artificial data on which it was trained. Importantly, even though the model was trained using noisy data, it maintained excellent prediction accuracy not only for noisy signals but also for clean data without noise contamination. This indicates that the model effectively avoided overfitting to noise and successfully captured the underlying structural response patterns, which is critical for its practical applicability in real-world scenarios, such as monitoring and decision-making in the context of NPP safety.

The validation process provides a comprehensive evaluation of the model's performance by covering a broad range of possible seismic scenarios. The ability to predict structural responses accurately under various seismic conditions ensures that the model can be confidently applied to enhance the safety and reliability of NPPs.

4.4 | Discussion

In this case study, physical sensors are assumed to be located at the same positions as the preselected nodes shown in Figure 7. The seismic response, which traditionally required direct measurement using multiple physical sensors, can now be accurately estimated with just a single precise seismometer by utilizing virtual sensor technology. One of the potential applications of such a virtual sensor system is to prioritize the locations of equipment that require urgent inspection after an earthquake, rather than conducting the sequential checks. Figure 14 shows an overview of virtualizing scheme of physical sensors in NPP and Figure 15a,b describes scenarios where the NPP experiences two earthquakes that were not used for training the virtual sensing model. Based on seismometer data, the model estimates responses at 139 locations within the NPP simultaneously. It then identifies and flags any locations that exceed predefined threshold values, which can be set by the administrator, and notifies them for immediate inspection. In Figure 15a, the threshold for all locations was set to 100.0, while in Figure 15b, it was set to 150.0. However, it is entirely possible to assign different thresholds for each location as needed. The red dots mark the locations currently monitored by the virtual sensing model, and locations identified as exceeding pre-defined thresholds were highlighted as yellow. Such applications of virtual sensors are expected to allow administrators to focus on the critical areas first, thereby enhancing the effectiveness in ensuring the safety and operational resilience of the NPP.

The virtual sensing model demonstrated strong robustness. It was trained on synthetic datasets with realistic noise levels (10 and 20 dB SNR) and maintained high accuracy under noisy conditions. This confirms the model's ability to suppress noise and provide reliable multi-location seismic response predictions. Rather than replacing physical sensors entirely, the model aims to supplement them by predicting acceleration responses at un-instrumented locations, particularly for critical equipment in auxiliary buildings. Assuming intact structural conditions, the model focuses on monitoring equipment behavior—not structural damage, making it highly applicable for rapid condition screening and prioritization of post-earthquake inspections.

In addition to robustness against noise, the model is optimized for computational efficiency. With 2.0 million parameters and multi-scale kernel configurations (sizes 100, 50, and 10), the model achieves an inference time of 3 s per prediction (covering 139 nodal responses over 3000-time steps) on a standard GPU (e.g., NVIDIA RTX 4090). The trained model contains approximately 2.0 million parameters, which can be efficiently run on even low-cost, consumer-grade GPUs with 3–4 GB of memory. This real-time inference capability aligns with the operational requirements of NPPs, where seismic response monitoring must be performed in real time, and post-event assessments are recommended to be completed within a few minutes to ensure effective decision-making and rapid inspection prioritization (Electric Power Research Institute, 2013; NRC, 2020).

Xu et al. (2021) proposed an LSTM-based framework for real-time seismic damage assessment, focusing on estimating building-level damage indices from ground motion. While effective for regional damage mapping, their model is trained on specific building portfolios and lacks scalability to high-resolution, multi-node structural response prediction. Zhou et al. (2024) introduced a physics-informed neural network (PINN) to predict structural responses by incorporating governing equations into the learning process. However, PINNs require intensive training for each output location due to the need for node-wise collocation and boundary conditions, making them computationally impractical for dense sensor networks. In contrast, the residual 1D CNN developed in this study directly predicts acceleration responses at multiple nodes simultaneously from a single seismometer. LSTM- and PINN-based models often involve high computational costs and require location-specific modeling, making them less suitable for large-scale, multi-location response prediction. Design of the proposed model, combined with weight sharing and residual connections, enables

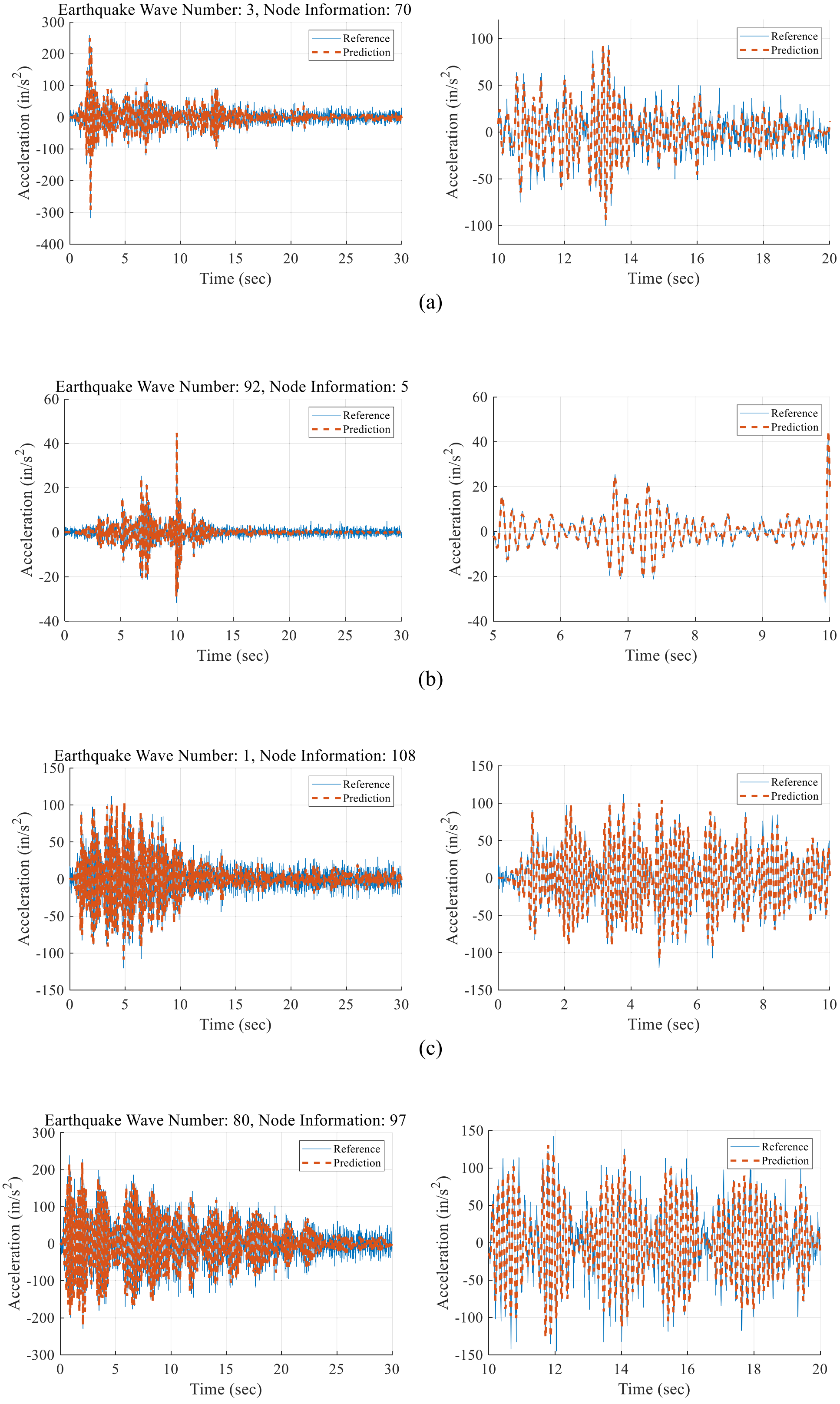

FIGURE 13 (a) and (b): Selected prediction results (left) and enlarged views (right) of Case 1 (i.e., NGA-West 2 database matching Regulatory Guide 1.60 spectrum), (c) and (d): selected prediction results (left) and enlarged views (right) of Case 2 (i.e., NGA-West 2 database matching Korean Uniform Hazard Spectrum [UHS]).

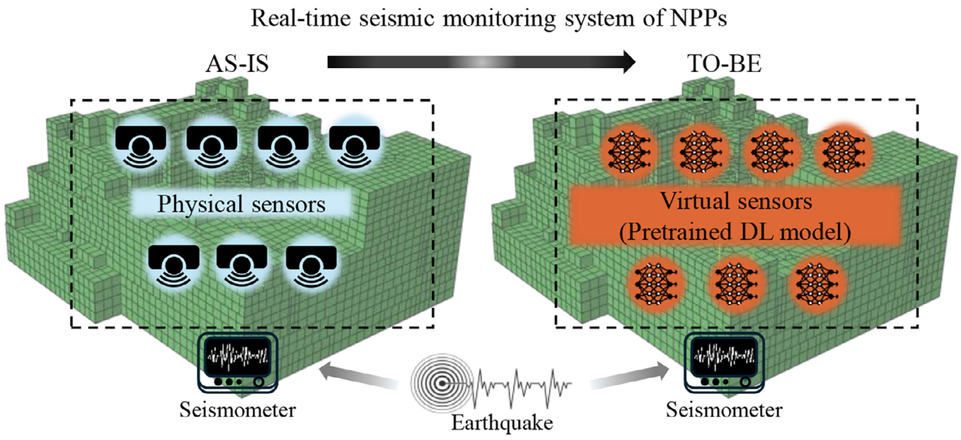

FIGURE 14 Overview of virtualizing scheme of physical sensors in nuclear power plants [NPPs].

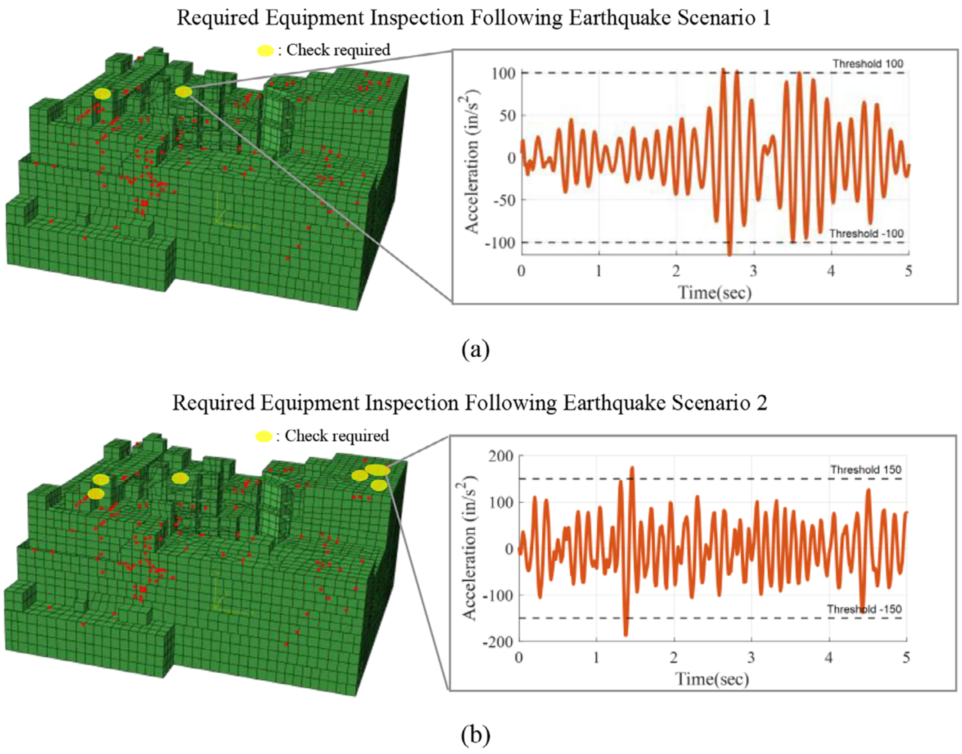

FIGURE 15 Locations highlighted in yellow, identified as exceeding a predefined threshold and an example prediction prioritized for urgent inspection in (a) Scenario 1 and (b) Scenario 2.

efficient and noise-tolerant prediction across all locations without the need to customize the model for each node. The proposed virtual sensing method combines robustness against noise, computational efficiency. This demonstrates its strong potential for real-world deployment in NPP monitoring systems.

Several challenges may arise depending on the specific application, although there were no critical issues within the scope of this study. Dataset shift due to changing structural or operational conditions may degrade model performance over time, requiring periodic revalidation (Moreno-Torres et al., 2012). Integration into existing safety systems is also complicated by data format inconsistencies and real-time constraints, with interoperability identified as a critical issue by the NRC (Yadav et al., 2021). In addition, sensor degradation under harsh environments, such as high radiation or thermal cycling, remains a known concern in NPP applications (Hossain et al., 2024). Also, the black-box nature of deep learning introduces risks under unseen or out-of-distribution conditions. To mitigate this, it is recommended to restrict the model's operational use to the trained domain, specifically, the elastic domain in this study, where its performance has been validated.

5 | CONCLUSION

In this study, the residual 1D CNN-based method for virtualizing physical sensors in NPPs was proposed. Given the critical role and seismic vulnerability of auxiliary-building critical equipment such as control cabinets and panels, the study addresses the limitations of traditional sensors including malfunctions, measurement errors, and maintenance challenges. By estimating seismic responses at multiple structural locations using only seismometer data, the proposed virtual sensing method provides a resilient and cost-effective alternative. It supports rapid post-earthquake prioritization of critical equipment inspections and serves as a complementary tool to FEM, enabling a synergistic approach.

To construct the virtualization model, the deep residual CNN was employed, effectively mitigating the vanishing gradient problem and enabling the extraction of complex seismic response patterns. The model was trained using synthetic earthquake data and rigorously validated under multiple real earthquake scenarios. For AEQ cases not used during training, the model achieved a mean mMAPE of 0.65% under noise-free conditions, 1.70% with 20 dB SNR, and 4.66% with 10 dB SNR, demonstrating strong robustness to noise contamination.

Validation using real earthquake events further confirmed the model's generalizability. When tested with NGA-West2 ground motions adjusted to match the NUREG 1.60 and Korean UHS, the model maintained low prediction errors. For Case 1, the mean mMAPE was 0.44% without noise, 1.19% with 20 dB SNR, and 3.30% with 10 dB SNR. For Case 2, the corresponding errors were 0.59%, 1.55%, and 4.23%, respectively. These results demonstrate that even under noise conditions, the model can accurately estimate seismic responses across all 139 locations simultaneously.

This study highlights several key contributions. First, it establishes a practical virtual sensing method capable of rapid equipment monitoring across complex NPP auxiliary structures. Second, it validates the resilience of the approach against realistic noise conditions, ensuring reliable performance even in field environments. Third, it demonstrates that high-fidelity seismic response prediction is achievable with minimal physical sensor infrastructure, supporting future applications in safety-critical infrastructure monitoring.

The primary objective of the proposed framework is to enable rapid estimation of potential damage to critical equipment (e.g., electrical cabinets) that may be affected even when the structural response remains within the elastic domain. This focus addresses a practical need in NPPs where conventional tools have been insufficient for efficiently computing seismic response histories at multiple locations. However, the model remains limited by its black-box nature (Gulgec et al., 2020) and potential dataset shift due to evolving structural conditions (Moreno-Torres et al., 2012), which may affect generalization. The model also does not explicitly consider FE modeling errors or potential simulation bias, which are important for deployment in real-world scenarios. These limitations highlight the importance of future research on FE model updating or data integration with field measurements. In addition, incorporating self-supervised pretraining on large-scale unlabeled vibration data (Rafiei et al., 2024) and uncertainty quantification techniques could further enhance generalizability and robustness under noisy or limited data conditions.

Overall, the proposed virtualization method offers a robust foundation for next-generation virtual sensing systems in NPPs. It enables continuous, accurate monitoring while substantially reducing installation and maintenance burdens, ultimately contributing to enhanced operational safety and resilience against seismic risks.

ACKNOWLEDGMENTS

This work was supported by the National Research Foundation of Korea (NRF) grant funded by the Korea government (MSIT; 2021R1C1C2008770). This work was also supported by the National Research Foundation of Korea (NRF) grant funded by the Korea government (MSIT; No. RS-2022-00144434).

REFERENCES

Alam, K. M. R., Siddique, N., & Adeli, H. (2020). A dynamic ensemble learning algorithm for neural networks. *Neural Computing and Applications*, *32*(10), 8675–8690.

Alonso, S., Morán, A., Pérez, D., Prada, M. A., Fuertes, J. J., & Dominguez, M. (2021). Virtual sensor for probabilistic estimation of the evaporation in cooling towers. *Integrated Computer-Aided Engineering*, *28*(4), 369–381.

Amezquita-Sanchez, J. P., Valtierra-Rodriguez, M., & Adeli, H. (2018). Wireless smart sensors for monitoring the health condition of civil infrastructure. *Scientia Iranica*, *25*(6), 2913–2925.

Ancheta, T. D., Darragh, R. B., Stewart, J. P., Seyhan, E., Silva, W. J., Chiou, B. S. J., Wooddell, K. E., Graves, R. W., Kottke, A. R., Boore, D. M., Kishida, T., & Donahue, J. L. (2014). NGA-West2 database. *Earthquake Spectra*, *30*(3), 989–1005.

Autorité de Sûreté Nucléaire (ASN). (2020). *ASN annual report on the state of nuclear safety and radiation protection in France in 2020*. https://www.french-nuclear-safety.fr/content/download/179293/file/ASN%20Report%20on%20the%20state%20of%20nuclear%20safety%20and%20radiation%20protection%20in%20France%20in%202020.pdf

Bai, S., Kolter, J. Z., & Koltun, V. (2018). *An empirical evaluation of generic convolutional and recurrent networks for sequence modeling*. arXiv. https://arxiv.org/abs/1803.01271

Bhatta, S., & Dang, J. (2024). Multiclass seismic damage detection of buildings using quantum convolutional neural network. *Computer-Aided Civil and Infrastructure Engineering*, *39*(3), 406–423.

Bigoni, C., Zhang, Z., & Hesthaven, J. S. (2020). Systematic sensor placement for structural anomaly detection in the absence of damaged states. *Computer Methods in Applied Mechanics and Engineering*, *371*, 113315.

Boore, D. M., & Goulet, C. A. (2019). The use of ground-motion simulations in seismic hazard analysis. *Earthquake Spectra*, *35*(2), 757–775.

Choi, I. K., Seo, J. M., & Choun, Y. S. (2003). Evaluation of high frequency ground motion effects on the seismic capacity of NPP equipments. *Transactions of the 17th International Conference on Structural Mechanics in Reactor Technology (SMiRT 17)*, Prague, Czech Republic.

Choi, Y., Nguyen, H. T., Han, T. H., Choi, Y., & Ahn, J. (2024). Sequence deep learning for seismic ground response modeling: 1D-CNN, LSTM, and transformer approach. *Applied Sciences*, *14*(15), 6658.

Choun, Y. S., & Kwon, T. H. (2018). Criteria for exceedance of operating basis earthquake based on the characteristics of site-specific ground motions. In transactions of the Korean Nuclear Society autumn meeting.

de Lautour, O. R., & Omenzetter, P. (2009). Prediction of seismic-induced structural damage using artificial neural networks. *Engineering Structures*, *31*(2), 600–606.

Electric Power Research Institute. (2013). *Seismic monitoring and safety assessment for nuclear power plants*. Report No. 3002000708, Electric Power Research Institute.

Farag, M. M., Sharaf, M. H., & Taloba, A. I. (2022). Short-time Fourier transform analysis in deep learning applications. *Signal, Image and Video Processing*, *16*(8), 2119–2127.

Gabriel, M., & Auer, T. (2023). LSTM deep learning models for virtual sensing of indoor air pollutants: A feasible alternative to physical sensors. *Buildings*, *13*(7), 1684.

Gao, H., Hu, G., Zhang, D., Jiang, W., Tse, K. T., Kwok, K. C. S., & Kareem, A. (2024). Urban wind field prediction based on sparse sensors and physics-informed graph-assisted auto-encoder. *Computer-Aided Civil and Infrastructure Engineering*, *39*(10), 1409–1430.

Gao, Y., Yang, J., Qian, H., & Mosalam, K. M. (2023). Multiattribute multitask transformer framework for vision-based structural health monitoring. *Computer-Aided Civil and Infrastructure Engineering*, *38*(17), 2358–2377.

Ghosh, J., Tonoli, A., & Amati, N. (2018). *A deep learning based virtual sensor for vehicle sideslip angle estimation: Experimental results*. SAE Technical Paper 2018-01-1089, SAE International.

Gulgec, N. S., Takáč, M., & Pakzad, S. N. (2020). Structural sensing with deep learning: Strain estimation from acceleration data for fatigue assessment. *Computer-Aided Civil and Infrastructure Engineering*, *35*(12), 1349–1364.

Hampshire, T. A., & Adeli, H. (2000). Monitoring the behavior of steel structures using distributed optical fiber sensors. *Journal of Constructional Steel Research*, *53*(3), 267–281.

He, K., Zhang, X., Ren, S., & Sun, J. (2016). Deep residual learning for image recognition. In *Proceedings of the IEEE Conference on Computer Vision and Pattern Recognition*, Las Vegas, NV (pp. 770–778).

Hossain, R. B., Kobayashi, K., & Alam, S. B. (2024). Sensor degradation in nuclear reactor pressure vessels: The overlooked factor in remaining useful life prediction. *npj Materials Degradation*, *8*(1), 71.

Huang, B., Lu, W., & Mosalam, K. M. (2017). Shaking table tests of the cable tray system in nuclear power plants. *Journal of Performance of Constructed Facilities*, *31*(4), 04017042.

Huang, C. S., Hung, S. L., Wen, C. M., & Tu, T. T. (2003). A neural network approach for structural identification and diagnosis of a building from seismic response data. *Earthquake Engineering & Structural Dynamics*, *32*(2), 187–206.

Huang, P., & Chen, Z. (2021). Deep learning for nonlinear seismic responses prediction of subway station. *Engineering Structures*, *244*, 112735.

Ige, A. O., & Sibiya, M. (2024). State-of-the-art in 1D convolutional neural networks: A survey. *IEEE Access*, *12*, 123456–123478.

International Atomic Energy Agency (IAEA). (2007). *IAEA mission report: Preliminary findings and lessons learned from the 16 July 2007earthquake at Kashiwazaki-Kariwa nuclear power plant (Vol. 1)*. IAEA.

International Atomic Energy Agency. (2018). *Advanced wireless communication in the instrumentation and control systems of nuclear power plant*. IAEA-TECDOC-1869. IAEA.

Ioffe, S., & Szegedy, C. (2015). Batch normalization: Accelerating deep network training by reducing internal covariate shift. In *Proceedings of the 32nd International Conference on Machine Learning*, Lille, France (pp. 448–456).

Japan Nuclear Safety Institute. (2011). Responses to the Tohoku–Pacific Ocean Earthquake and Tsunami at the Onagawa Nuclear Power Station and Tokai No.2 Power Station. https://www.genanshin.jp/english/archive/disastersitereaction/data/report_OnTk.pdf

Kaewnuratchadasorn, C., Wang, J., & Kim, C.-W. (2024a). Neural operator for structural simulation and bridge health monitoring. *Computer-Aided Civil and Infrastructure Engineering*, *39*(6), 872–890.

Kassawara, R. (2012). *Seismic walkdown guidance: For resolution of Fukushima near-term task force recommendation 2.3: Seismic (Draft 5 Report)*. Report No. 1025286, Electric Power Research Institute (EPRI).

Kiranyaz, S., Avci, O., Abdeljaber, O., Ince, T., Gabbouj, M., & Inman, D. J. (2021). 1D convolutional neural networks and applications: A survey. *Mechanical Systems and Signal Processing*, *151*, 107398.

Martin, D., Kühl, N., & Satzger, G. (2021). Virtual sensors. *Business & Information Systems Engineering*, *63*(3), 315–323.

Miao, Y., Kang, H., Hou, W., Liu, Y., Zhang, Y., & Wang, C. (2024). A response-compatible ground motion generation method using physics-guided neural networks. *Computer-Aided Civil and Infrastructure Engineering*, *39*(15), 2350–2366.

Mittelman, R. (2015). *Time-series modeling with undecimated fully convolutional neural networks*. arXiv. https://arxiv.org/abs/1508.00317

Moreau, D., Cazzolato, B., Zander, A., & Petersen, C. (2008). A review of virtual sensing algorithms for active noise control. *Algorithms*, *1*(2), 69–99.

Moreno-Torres, J. G., Raeder, T., Alaiz-Rodríguez, R., Chawla, N. V., & Herrera, F. (2012). A unifying view on dataset shift in classification. *Pattern Recognition*, *45*(1), 521–530.

Morfidis, K., & Kostinakis, K. (2017). Seismic parameters' combinations for the optimum prediction of the damage state of R/C buildings using neural networks. *Advances in Engineering Software*, *106*, 1–16.

Oh, B. K., Park, Y., & Park, H. S. (2020). Seismic response prediction method for building structures using convolutional neural network. *Structural Control and Health Monitoring*, *27*(5), e2519.

Park, H., Kim, Y., & Lee, J. (2021). Influence of frequency content of ground motions on seismic fragility of equipment in nuclear power plant. *Engineering Structures*, *242*, 112603.

Patrizi, G., Bartolini, A., Ciani, L., Gallo, V., Sommella, P., & Carratù, M. (2022). A virtual soil moisture sensor for smart farming using deep learning. *IEEE Transactions on Instrumentation and Measurement*, *71*, 2502310.

Pereira, D. R., Piteri, M. A., Souza, A. N., Papa, J., & Adeli, H. (2020). FEMa: A finite element machine for fast learning. *Neural Computing and Applications*, *32*(10), 6393–6404.

Rafiei, M. H., & Adeli, H. (2017). A new neural dynamic classification algorithm. *IEEE Transactions on Neural Networks and Learning Systems*, *28*(12), 3074–3083.

Rafiei, M. H., Gauthier, L. V., Adeli, H., & Takabi, D. (2024). Self-Supervised Learning for Electroencephalography. *IEEE Transactions on Neural Networks and Learning Systems*, *35*(2), 1457–1471. https://doi.org/10.1109/TNNLS.2022.3190448

Ramachandran, P., Zoph, B., & Le, Q. V. (2017). *Searching for activation functions*. arXiv. https://arxiv.org/abs/1710.05941

Rashvand, H. F., Abedi, A., Alcaraz-Calero, J. M., Mitchell, P. D., & Mukhopadhyay, S. C. (2014). Wireless sensor systems for space and extreme environments: A review. *IEEE Sensors Journal*, *14*(11), 3955–3970.

Rezaeian, S., & Der Kiureghian, A. (2010). Simulation of synthetic ground motions for specified earthquake and site characteristics. *Earthquake Engineering & Structural Dynamics*, *39*(10), 1155–1180.

Santurkar, S., Tsipras, D., Ilyas, A., & Madry, A. (2018). How does batch normalization help optimization? In S. Bengio, H. Wallach, H. Larochelle, K. Grauman, N. Cesa-Bianchi, & R. Garnett (Eds.), *Advances in neural information processing systems 31* (pp. 2483–2493). Curran Associates.

Sercel. (2023). *A high sensitivity MEMS-based accelerometer* [White paper]. Sercel.

Shabbir, K., Noureldin, M., & Sim, S. H. (2025). Data-driven model for seismic assessment, design, and retrofit of structures using explainable artificial intelligence. *Computer-Aided Civil and Infrastructure Engineering*, *40*(3), 281–300.

Shi, Y., Lavrentiadis, G., Asimaki, D., Ross, Z. E., & Azizzadenesheli, K. (2024). Broadband ground-motion synthesis via generative adversarial neural operators: Development and validation. *Bulletin of the Seismological Society of America*, *114*(4), 2151–2171.

Shin, K.-H., Kim, C., Nam, S.-H., Park, S.-J., & Yoo, S.-S. (2018). Estimation method of predicted time series data based on absolute maximum value. *Journal of Energy Engineering*, *27*(4), 103–110.

Sirca, G. F., Jr., & Adeli, H. (2004). A neural network-wavelet model for generating artificial accelerograms. *International Journal of Wavelets, Multiresolution and Information Processing*, *2*(3), 217–235.

Stavropoulos, G., Violos, J., Tsanakas, S., & Leivadeas, A. (2023). Enabling artificial intelligent virtual sensors in an IoT environment. *Sensors*, *23*(3), 1328.

Sun, S.-B., He, Y.-Y., Zhou, S.-D., & Yue, Z.-J. (2017). A data-driven response virtual sensor technique with partial vibration measurements using convolutional neural network. *Sensors*, *17*(12), 2888.

Tezcan, J., & Marin-Artieda, C. C. (2018). Least-square-support-vector-machine-based approach to obtain displacement from measured acceleration. *Advances in Engineering Software*, *115*, 357–362.

U.S. Nuclear Regulatory Commission (NRC). (2011). *North Anna Power Station, Units 1 and 2–Technical evaluation report*. NUREG Report No. ML11308B406. US Nuclear Regulatory Commission.

U.S. Nuclear Regulatory Commission. (2014). *Design response spectra for seismic design of nuclear power plants* (Regulatory Guide 1.60, Revision 2). US Nuclear Regulatory Commission.

U.S. Nuclear Regulatory Commission. (2020). *Standard review plan for the review of safety analysis reports for nuclear power plants (NUREG-0800)*. US Nuclear Regulatory Commission.

Wüest, T., Heider, P., & Yue, Z. J. (2024). *Virtual sensing for real-time degradation monitoring of nuclear systems leveraging DeepONet*. arXiv. https://arxiv.org/abs/2403.12345

Xu, Y., Lu, X., Cetiner, B., & Taciroglu, E. (2021). Real-time regional seismic damage assessment framework based on long short-term memory neural network. *Computer-Aided Civil and Infrastructure Engineering*, *36*(4), 504–521.

Yadav, V., Agarwal, V., Gribok, A. V., Hays, R. D., Pluth, A. J., Ritter, C. S., Zhang, H., Jain, P. K., Ramuhalli, P., Eskins, D., Carlson, J., Gascot, R. L., Ulmer, C., & Iyengar, R. (2021). *Technical challenges and gaps in digital-twin-enabling technologies for nuclear reactor applications*. Idaho National Laboratory. https://www.nrc.gov/docs/ML2136/ML21361A261.pdf

Yoon, S. (2022). Virtual sensing in intelligent buildings and digitalization. *Automation in Construction*, *143*, 104578.

Zaidan, M. A., Motlagh, N. M., Fung, P. L., Lu, D., Timonen, H., Kuula, J., Niemi, J. V., Tarkoma, S., Petäjä, T., Kulmala, M., & Hussein, T. (2020). Intelligent calibration and virtual sensing for integrated low-cost air quality sensors. *IEEE Sensors Journal*, *20*(22), 13638–13652.

Zhang, R., Chen, Z., Chen, S., Zheng, J., Büyüköztürk, O., & Sun, H. (2019). Deep long short-term memory networks for nonlinear structural seismic response prediction. *Computers & Structures*, *220*, 55–68.

Zhang, Y., & Wang, L. (2023). Damage localization using a deep learning-based response reconstruction method under noisy measurements. *Computers & Structures*, *293*, 107042.

Zhou, Y., Meng, S., Lou, Y., & Kong, Q. (2024). Physics-informed deep learning-based real-time structural response prediction method. *Engineering*, *35*, 140–157.

How to cite this article: Lee, J., Lee, S., Lee, Y.-J., & Lee, J. (2025). Virtual sensing of seismic floor responses for rapid prioritization of critical equipment inspection in nuclear power plants. *Computer-Aided Civil and Infrastructure Engineering*, 1–20. https://doi.org/10.1111/mice.70051

APPENDIX

Detailed information of real earthquake data downloaded from NGA-WEST 2 database used to match the NRC 1.60 spectrum and Korean UHS (Table A1).

TABLE A1 Detailed information of earthquake data used in Sections 4.1 and 4.2 for validating the trained deep learning model.

No.	Earthquake name	Year	Station Name	Magnitude	Case 1	Case 2
1	"Helena_ Montana-01"	1935	"Carroll College"	6	O	O
2	"Helena_ Montana-02"	1935	"Helena Fed Bldg"	6	O	O
3	"Humbolt Bay"	1937	"Ferndale City Hall"	5.8	O	O
4	"Imperial Valley-01"	1938	"El Centro Array #9"	5	X	O
5	"Northwest Calif-01"	1938	"Ferndale City Hall"	5.5	O	O
6	"Imperial Valley-02"	1940	"El Centro Array #9"	6.95	O	O
7	"Northwest Calif-02"	1941	"Ferndale City Hall"	6.6	O	O
8	"Northern Calif-01"	1941	"Ferndale City Hall"	6.4	O	O
9	"Borrego"	1942	"El Centro Array #9"	6.5	O	O
10	"Imperial Valley-03"	1951	"El Centro Array #9"	5.6	O	O
11	"Northwest Calif-03"	1951	"Ferndale City Hall"	5.8	O	O
12	"Kern County"	1952	"LA—Hollywood Stor FF"	7.36	O	O
13	"Kern County"	1952	"Pasadena—CIT Athenaeum"	7.36	O	O
14	"Kern County"	1952	"Santa Barbara Courthouse"	7.36	O	O
15	"Kern County"	1952	"Taft Lincoln School"	7.36	O	O
16	"Northern Calif-02"	1952	"Ferndale City Hall"	5.2	O	O
17	"Southern Calif"	1952	"San Luis Obispo"	6	O	O
18	"Imperial Valley-04"	1953	"El Centro Array #9"	5.5	O	O
19	"Central Calif-01"	1954	"Hollister City Hall"	5.3	O	O
20	"Northern Calif-03"	1954	"Ferndale City Hall"	6.5	O	O
21	"Imperial Valley-05"	1955	"El Centro Array #9"	5.4	O	O
22	"El Alamo"	1956	"El Centro Array #9"	6.8	O	O
23	"San Francisco"	1957	"Golden Gate Park"	5.28	O	O
24	"Central Calif-02"	1960	"Hollister City Hall"	5	O	O
25	"Northern Calif-04"	1960	"Ferndale City Hall"	5.7	O	O
26	"Hollister-01"	1961	"Hollister City Hall"	5.6	O	O
27	"Hollister-02"	1961	"Hollister City Hall"	5.5	O	O
28	"Parkfield"	1966	"Cholame—Shandon Array #12"	6.19	O	O
30	"Parkfield"	1966	"Cholame—Shandon Array #5"	6.19	O	O
31	"Parkfield"	1966	"Cholame—Shandon Array #8"	6.19	O	O
32	"Parkfield"	1966	"San Luis Obispo"	6.19	O	O
33	"Parkfield"	1966	"Temblor pre-1969"	6.19	O	O
34	"Northern Calif-05"	1967	"Ferndale City Hall"	5.6	O	O
35	"Northern Calif-06"	1967	"Hollister City Hall"	5.2	O	O
36	"Borrego Mtn"	1968	"El Centro Array #9"	6.63	O	O
37	"Borrego Mtn"	1968	"LA—Hollywood Stor FF"	6.63	O	X
38	"Borrego Mtn"	1968	"LB—Terminal Island"	6.63	O	X
39	"Borrego Mtn"	1968	"Pasadena—CIT Athenaeum"	6.63	O	O
40	"Borrego Mtn"	1968	"San Onofre—So Cal Edison"	6.63	X	O

(Continues)

TABLE A1 (Continued)

No.	Earthquake name	Year	Station Name	Magnitude	Case 1	Case 2
41	“Lytle Creek”	1970	“Castaic—Old Ridge Route”	5.33	O	O
42	“Lytle Creek”	1970	“Cedar Springs Pumphouse”	5.33	O	O
43	“Lytle Creek”	1970	“Cedar Springs_ Allen Ranch”	5.33	O	O
44	“Lytle Creek”	1970	“Colton—So Cal Edison”	5.33	X	O
45	“Lytle Creek”	1970	“Devil’s Canyon”	5.33	O	O
46	“Lytle Creek”	1970	“LA—Hollywood Stor FF”	5.33	O	O
47	“Lytle Creek”	1970	“Lake Hughes #1”	5.33	O	O
48	“Lytle Creek”	1970	“Puddingstone Dam (Abutment)”	5.33	O	O
49	“Lytle Creek”	1970	“Santa Anita Dam”	5.33	O	O
50	“Lytle Creek”	1970	“Wrightwood - 6074 Park Dr”	5.33	O	O
51	“San Fernando”	1971	“2516 Via Tejon PV”	6.61	O	O
52	“San Fernando”	1971	“Anza Post Office”	6.61	O	O
53	“San Fernando”	1971	“Bakersfield—Harvey Aud”	6.61	O	O
54	“San Fernando”	1971	“Borrego Springs Fire Sta”	6.61	O	O
55	“San Fernando”	1971	“Buena Vista—Taft”	6.61	O	O
56	“San Fernando”	1971	“Carbon Canyon Dam”	6.61	O	O
57	“San Fernando”	1971	“Castaic—Old Ridge Route”	6.61	O	O
58	“San Fernando”	1971	“Cedar Springs Pumphouse”	6.61	O	O
59	“San Fernando”	1971	“Cedar Springs_ Allen Ranch”	6.61	O	O
60	“San Fernando”	1971	“Cholame—Shandon Array #2”	6.61	O	X
61	“San Fernando”	1971	“Cholame—Shandon Array #8”	6.61	O	O
62	“San Fernando”	1971	“Colton—So Cal Edison”	6.61	O	O
63	“San Fernando”	1971	“Fairmont Dam”	6.61	O	O
64	“San Fernando”	1971	“Fort Tejon”	6.61	O	O
65	“San Fernando”	1971	“Gormon—Oso Pump Plant”	6.61	O	O
66	“San Fernando”	1971	“Hemet Fire Station”	6.61	O	O
67	“San Fernando”	1971	“Isabella Dam (Aux Abut)”	6.61	O	O
68	“San Fernando”	1971	“LA—Hollywood Stor FF”	6.61	O	O
69	“San Fernando”	1971	“LB—Terminal Island”	6.61	O	O
70	“San Fernando”	1971	“Lake Hughes #1”	6.61	O	O
71	“San Fernando”	1971	“Lake Hughes #12”	6.61	O	O
72	“San Fernando”	1971	“Lake Hughes #4”	6.61	O	O
73	“San Fernando”	1971	“Lake Hughes #9”	6.61	O	O
74	“San Fernando”	1971	“Maricopa Array #1”	6.61	O	X
75	“San Fernando”	1971	“Maricopa Array #2”	6.61	O	X
76	“San Fernando”	1971	“Maricopa Array #3”	6.61	O	X
77	“San Fernando”	1971	“Pacoima Dam (upper left abut)”	6.61	O	O
78	“San Fernando”	1971	“Palmdale Fire Station”	6.61	O	O
79	“San Fernando”	1971	“Pasadena—CIT Athenaeum”	6.61	O	O
80	“San Fernando”	1971	“Pasadena—Old Seismo Lab”	6.61	O	O
81	“San Fernando”	1971	“Pearblossom Pump”	6.61	O	O
82	“San Fernando”	1971	“Port Hueneme”	6.61	O	O
83	“San Fernando”	1971	“Puddingstone Dam (Abutment)”	6.61	O	O
84	“San Fernando”	1971	“San Diego Gas & Electric”	6.61	O	X
85	“San Fernando”	1971	“San Juan Capistrano”	6.61	O	O

(Continues)

TABLE A1 (Continued)

No.	Earthquake name	Year	Station Name	Magnitude	Case 1	Case 2
86	“San Fernando”	1971	“San Onofre—So Cal Edison”	6.61	O	O
87	“San Fernando”	1971	“Santa Anita Dam”	6.61	O	O
88	“San Fernando”	1971	“Santa Felita Dam (Outlet)”	6.61	O	O
89	“San Fernando”	1971	“Tehachapi Pump”	6.61	O	O
90	“San Fernando”	1971	“UCSB—Fluid Mech Lab”	6.61	O	O
91	“San Fernando”	1971	“Upland—San Antonio Dam”	6.61	O	O
92	“San Fernando”	1971	“Wheeler Ridge—Ground”	6.61	O	O
93	“San Fernando”	1971	“Whittier Narrows Dam”	6.61	O	O
94	“San Fernando”	1971	“Wrightwood - 6074 Park Dr”	6.61	O	O
95	“Managua_ Nicaragua-01”	1972	“Managua_ ESSO”	6.24	O	O
96	“Managua_ Nicaragua-02”	1972	“Managua_ ESSO”	5.2	O	O
97	“Point Mugu”	1973	“Port Hueneme”	5.65	X	O
98	“Hollister-03”	1974	“Gilroy Array #1”	5.14	O	O
99	“Hollister-03”	1974	“Hollister City Hall”	5.14	O	O
100	“Hollister-03”	1974	“San Juan Bautista_ 24 Polk St”	5.14	O	O
101	“Northern Calif-07”	1975	“Cape Mendocino”	5.2	O	O